



The investigation on the fabrication and microstructure of NbTi-(NbTi)C Fe-based composite

Jian-lei Zhu^{a,b}, Li-sheng Zhong^{a,b,*}, Yun-hua Xu^{a,b,**}, Shao-xiong zhang^a, Zheng-xin Lu^{a,c}

^a School of Materials Science and Engineering, Xi'an University of Technology, Xi'an, 710048, PR China

^b International Research Center for Composite and Intelligent Manufacturing Technology, Xi'an University of Technology, Xi'an, 710048, PR China

^c Xi'an Zhitong Automation Technology Ltd. Co., Xi'an, 710048, PR China

ARTICLE INFO

Keywords:

Metal matrix composites
(NbTi)C
Microstructure
High hardness

ABSTRACT

NbTi-(NbTi)C Fe-based composites are fabricated by *in-situ* diffusion reaction. The locally reinforced (NbTi)C cermet layer formed by carrying out the reaction of $C + \beta\text{-NbTi} \rightarrow (\text{NbTi})\text{C}$, which resulted in the formation of the core-annular shell structure with a ductile core (NbTi) and high hardness annular shell (cermet layer). The (NbTi)C cermet layer is composed of two zones, where ZoneI, near the GCI, is composed of micron and sub-micron-sized particles; and ZoneII, near the remnant $\beta\text{-NbTi}$, is composed of sub-micron-sized particles. The detailed microstructural, elemental and morphological analysis has been carried out to unveil the phase distribution and microstructural changes in the (NbTi)C cermet layer. The results reveal that the cermet layer consists of (NbTi)C particles with different Ti/(Ti + Nb) ratios, ranging from 0.6308 to 0.8330, which have different morphology: the fusiform particles and near spherical or cubic particles. Moreover, the nanoindentation results of (NbTi)C layer indicate that the maximum hardness and elastic modulus is 31.43 GPa and 473.11 GPa, respectively. It is worth mention that the remnant $\beta\text{-NbTi}$ and $\alpha\text{-Fe}$ phases, surrounding the (NbTi)C cermet layer, render high plasticity. Therefore, the combination of $\beta\text{-NbTi}$, $\alpha\text{-Fe}$ and (NbTi)C phases can effectively improve the hardness and plasticity of as-prepared composites.

1. Introduction

Metallic carbides render several superior characteristics, such as high strength, high hardness and high melting point, due to the character of covalent bond. Among different metal carbides, titanium carbide (TiC) and niobium carbide (NbC) have gained significant research focus due to their excellent mechanical properties and low density. Therefore, TiC and NbC are introduced into the metal matrix composites as the reinforcements [1–4] to improve their hardness, wear resistance, elastic modulus and high-temperature performance. Recently, a large number of studies have demonstrated the fabrication of carbide-reinforced cermet composites [5–7] for a wide range of applications, such as high-temperature materials and cemented carbides. However, the mechanical properties of the carbides and structural stability of resulting carbide-reinforced cermet composites should be further improved for advanced applications.

The presence of carbides enhances the mechanical properties of carbide-reinforced cermet composites by fine-grain strengthening and solid-solution strengthening, whereas the high volume fraction of

cermet can also enhance the hardness and wear resistance of carbide-reinforced cermet composites. Therefore, the hardness of carbides can be modulated by altering the synthesis procedure and carbide composition. Moreover, the carbide-reinforced cermet composites can be mainly prepared by using laser cladding [8,9], powder-sintering [10,11] and *in-situ* diffusion reaction [12–15]. For instance, Cao et al. [9] have prepared a vanadium-containing hard composite coating by laser cladding the prefabricated mixture of V, Cr, Mo, Ti and Nb powders on the plastic iron matrix and demonstrated a significantly improved hardness of the outer layer and the intermediate melting zone. The highest hardness of the coating was 960 HV_{0.1}. Furthermore, Jung et al. [10] utilized powder sintering route to synthesize (Ti,W)C carbides from the (Ti,W)C solid solution power at 1510 °C. The resulting (Ti,W)C carbides exhibited high density, excellent hardness (19–21 GPa) and desirable fracture toughness (6.4–7.7 MPa m^{-1/2}). However, the grain size of (Ti,W)C carbides increased due to the high sintering temperature, which suppressed the fine-grain strengthening effect. Our group synthesized a variety of carbide-reinforced cermet composites by using *in-situ* solid-phase diffusion reaction [12–16].

* Corresponding author. Xi'an University of Technology, 5 Jinhua Road, Xi'an, 710048, PR China.

** Corresponding author. Xi'an University of Technology, 5 Jinhua Road, Xi'an, 710048, PR China.

E-mail addresses: zhonglisheng@xaut.edu.cn (L.-s. Zhong), xuh_2000@126.com (Y.-h. Xu).

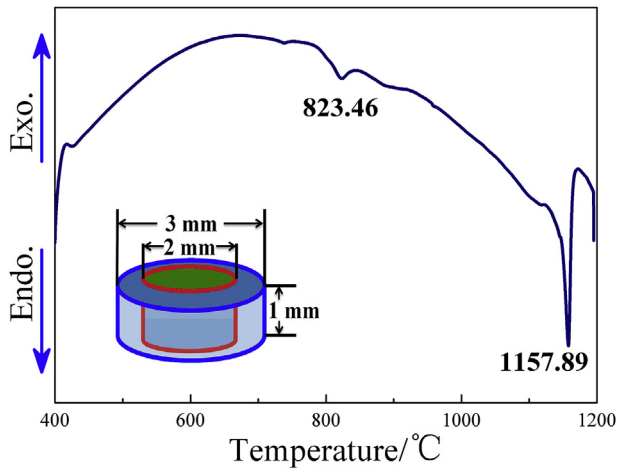


Fig. 1. The DSC curve and schematic illustration of the NbTi/GCI precursor.

Compared with laser cladding and powder sintering methods, *in-situ* solid-phase diffusion reaction technology renders micron- to nano-sized particles, clean reaction interface, high volume fraction of reinforcements and gradient structure, which provide high hardness and excellent wear resistance.

Among several reported carbide-reinforced ceramic composites, NbC and TiC cermet exhibit the highest hardness values of 23.5 GPa [12] and 27.7 GPa [13], respectively. In the case of multiphase carbides, the properties of (NbTi)C carbides have been investigated by First-principles calculations based on density functional theory (DFT). Zhao et al. [17] have demonstrated that the lattice constant and formation energy of (NbTi)C decrease with the decrease of Ti content. With the change of Nb/Ti ratio, the theoretical hardness of (Nb_{0.25}Ti_{0.75})C carbide is 28.51 GPa, whereas the theoretical hardness of NbC and TiC phases is 22.69 GPa and 25.78 GPa, respectively.

Therefore, we aimed to synthesize high hardness (NbTi)C ceramic

Table 1

The elemental composition of different regions marked in Figs. 2 and 3 (at. %).

Elements	C	Ti	Nb	Fe	Ti/(Ti + Nb)
A	30.81	38.51	23.99	3.44	0.62
B	60.96	30.25	8.20	0.59	0.79
C	64.47	28.13	6.11	1.28	0.82
D	70.61	15.71	10.82	2.86	0.59
E	55.24	37.42	7.34		0.84
F	82.30	13.62	4.02		0.77
Raw materials	–	70.34	29.65	–	0.70

composites by combining the advantages of *in-situ* diffusion reaction and solution strengthening of (NbTi)C carbide. Herein, both of the high carbon concentration of gray cast iron (GCI) and strong carbide formation characteristics of Ti and Nb are utilized to fabricate (NbTi)C cermet by *in-situ* diffusion reaction. The as-prepared (NbTi)C cermet exhibited core-annular shell structure, excellent bonding interface, high hardness and desirable elastic modulus. In this paper, the changes in microstructure, morphology, lattice constant and hardness of (NbTi)C cermet have been systematically investigated.

2. Materials and methods

2.1. Raw materials and preparation

A high-temperature TiNb alloy (43.95 wt % Nb, 53.36 wt % Ti, 0.67 wt % C, 2.0 wt % Si and a trace amount of Fe), with dimensions of $\Phi 1 \times 10$ mm, was used as the wire. The gray cast iron (GCI) (3.25 wt % C, 2.38 wt % Si, 0.56 wt % Mn, 0.014 wt % S and balance Fe), with dimensions of $10 \times 10 \times 10$ mm, was used as the matrix. The holes of $\Phi 1 \times 10$ mm were drilled in the GCI matrix. The NbTi wire and GCI were ultrasonically cleaned in nitric acid solution and acetone for 5 min and 10 min, respectively. Interference fitting of NbTi wires and holes was designed and, then, NbTi wires were pressed into the holes to keep the surface of NbTi wire and inner wall of GCI holes contacting closely.

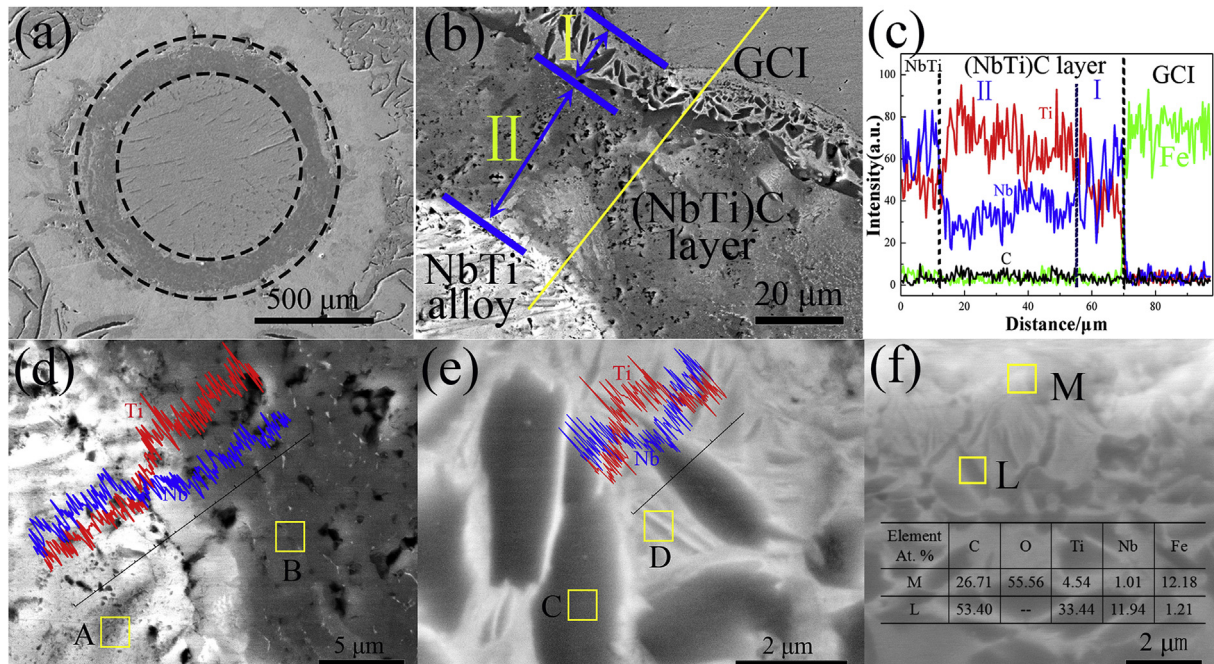


Fig. 2. SEM images of different micro-regions and element distribution of the sample produced in argon gas furnace: (a) the SEM image of cross-section; (b) the high-magnification images of cross-section; (c) element distribution along the yellow line marked in (b); (d) SEM image of the inner interface between NbTi and (NbTi)C cermet layer; (e) SEM images of zoned (NbTi)C cermet layer. The element distribution of Ti (red) and Nb (blue) on the inner interface and a single particle is inserted in (d) and (e), respectively. (f) the cross-sectional SEM image of the sample produced in vacuum box furnace. (For interpretation of the references to color in this figure legend, the reader is referred to the Web version of this article.)

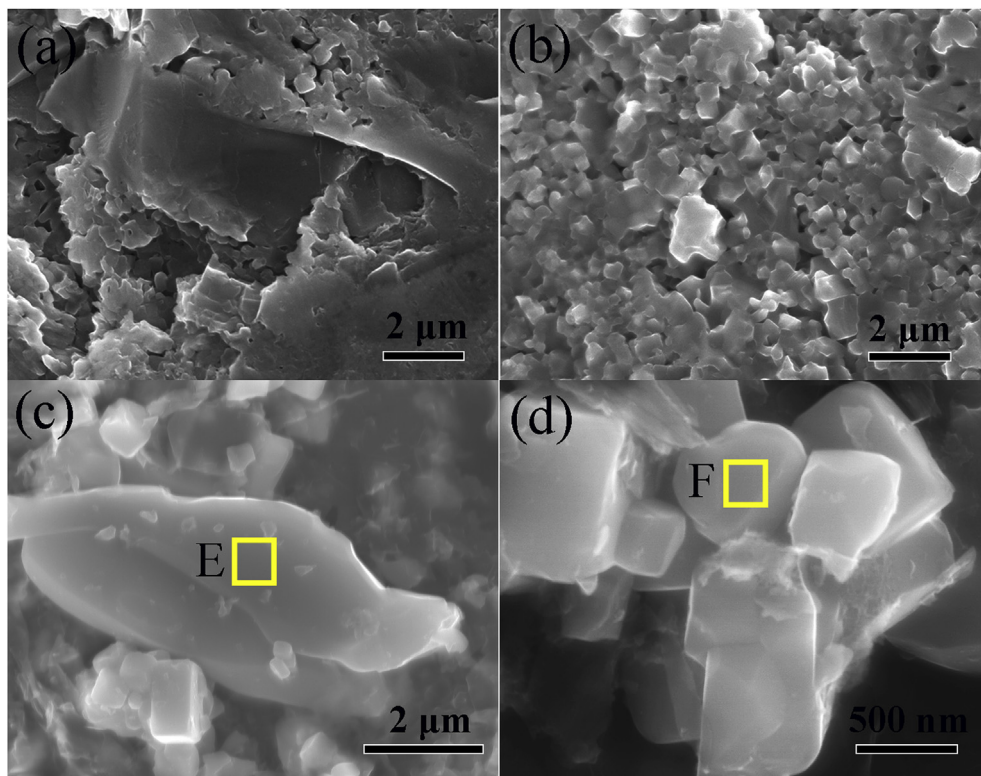


Fig. 3. The morphology of different types of particles in (a) Zone-I and (b) Zone-II obtained after radial compression of (NbTi)C cermet layer. The different dimensional morphology of the (c) fusiform and (d) near-spherical or cubic particles, extracted from (NbTi)C cermet layer after hydrochloric etching.

Lastly, the as-prepared precursors were coated with graphite paper, and then placed in a tube furnace under argon atmosphere with a flow rate of 5 mL/min and a vacuum furnace with a vacuum degree of 0.05 MPa, respectively. Inert Argon gas and vacuum environment are used to isolate samples from air and protect samples, and the residual waste gas is harmless and will not pollute the environment during the preparation process. The preparation method of the precursor is similar to the precursor synthesis of Ti-TiC-Fe composites [14].

Fig. 1 presents the DSC curve and the schematic illustration of the NbTi + GCI precursor. The DSC curve exhibited an endothermic peak at 1157.89 °C, corresponding to eutectic temperature. The carbon content in GCI was 3.25 wt %, which belongs to the hypoeutectic iron according to the Fe-C phase diagram. Owing to the influence of Si, Mn, Ti and Nb in the precursor, the endothermic peak expresses the eutectic temperature of the given reaction: $L + \gamma \rightarrow \text{Fe}_3\text{C} + \gamma + \text{L}_d$. Herein, the formation of cermet depends on the diffusion of C atoms into NbTi, which is significantly influenced by temperature. Therefore, a high diffusion rate of C atoms can be obtained by increasing the temperature. However, the reaction temperature should remain lower than the melting point of GCI. Hence, the *in-situ* diffusion reaction was carried out at 1150 °C for 6 h, followed by heating at 700 °C for 1 h. Then, the samples were furnace-cooled to room temperature.

2.2. Characterization

The cross-section of samples were polished for microstructures analysis. Also, the samples were longtime soaked in the concentrated hydrochloric acid to extract the (NbTi)C particles for the morphological analysis. The microstructure of the cermet layer and three-dimensional morphology of (NbTi)C particles were observed by scanning electron microscope (SEM, JSM-6700F, JEOL), equipped with an energy dispersive spectrometer (EDS Oxford, INCA). The field-emission transmission electron microscopy (TEM, JEM-3010) was carried out to characterize the microstructure and selected area electron diffraction

(SAED) patterns. The phase identification was carried out by using X-ray diffractometer (XRD, Smart Lab), equipped with Cu K α radiations, operating at 40 kV and 200 mA. The XRD patterns were recorded in the 2 θ range of 30°–90° at the scan rate of 3°/min. The hardness and elastic modulus were measured by using G200 nanoindentation tester (Agilent technologies). The test was carried out by using a Berkovich indenter on the polished cross-section under the load of 400 mN and dwelling time of 10 s.

3. Results and discussion

The precursors were heated in furnaces at 1150 °C for 6 h to carry out *in-situ* solid-phase diffusion reaction. Owing to the higher diffusion rate of C than Fe, Ti, and Nb [18], C atoms diffused into β -NbTi solid phase and reacted with Ti and Nb to form (Ti,Nb)C cermet layer. Finally, the samples were furnace-cooled to room temperature. The SEM images of the sample produced in argon gas furnace are shown in Fig. 2(a)–2(e). Fig. 2(f) is the cross-sectional image and the EDS result of the sample produced in vacuum furnace.

The cross-sectional morphology shown in Fig. 2(a) exhibited a core-shell structure, consisted of remnant β -NbTi wire core and (NbTi)C cermet annular shell. Fig. 2(c)–2(e) shows different micro-regions from the sample's cross-section and EDS line scans profile. SEM images show that the interface of NbTi/(NbTi)C cermet layer and the interface of (NbTi)C cermet layer/GCI, both of those are excellent bonding. Furthermore, the microstructure of (NbTi)C cermet layer can be divided into two zones, where Zone-I is a two-phase region with light- and dark-gray color particles and Zone-II is a region with same color particles (Fig. 2(b)). The EDS line scan shows obvious changes in Fe, Ti and Nb content at GCI/(NbTi)C-cermet layer interface, as shown in Fig. 2(c). The results prove that the diffusion of Fe atoms is limited to a narrow range during the heat diffusion process. Furthermore, in Zone-I, Nb content in the light-gray region is higher than the dark-gray region, whereas Ti content exhibits an opposite tendency. Therefore, the light-

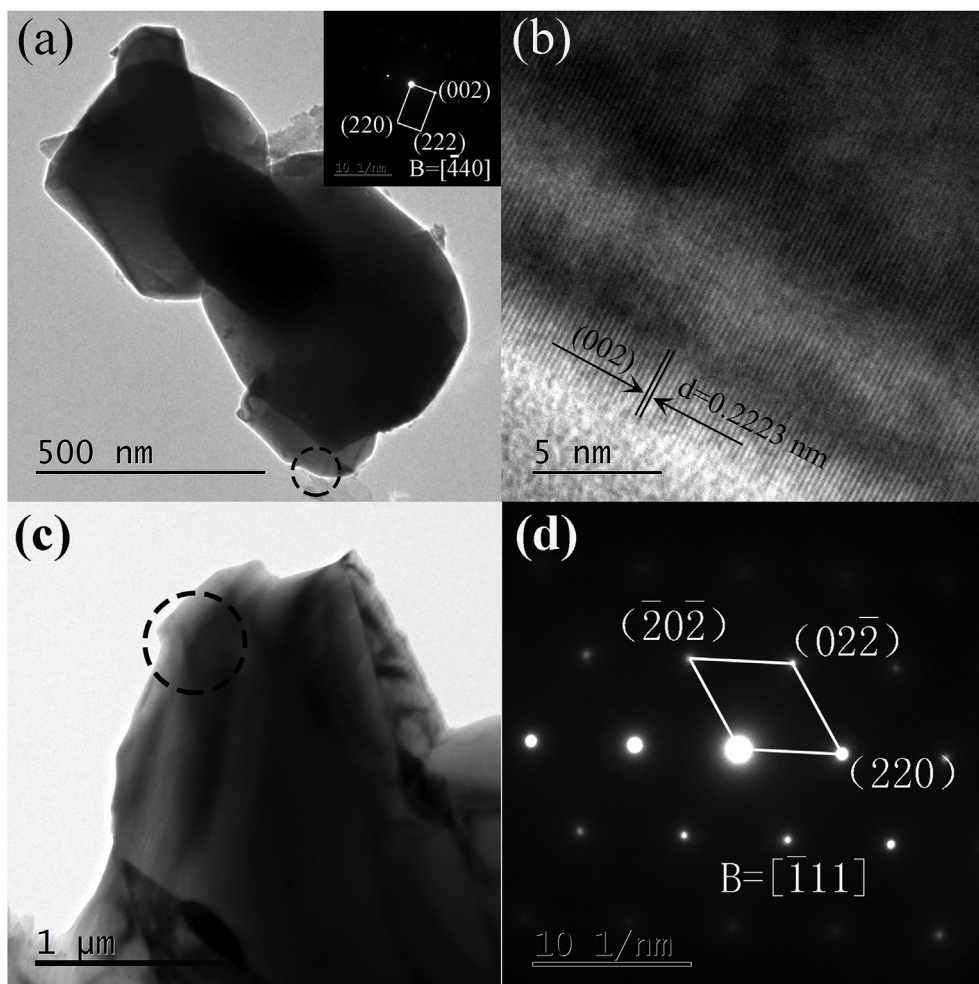


Fig. 4. (a) BF-TEM image of near-spherical (NbTi)C particles obtained by chemical extraction. The region of the selected area electron diffraction pattern marked with the circle. The SAED pattern (inserted in (a)) and (b) HRTEM image was collected from the region marked with a circle in (a). (c) BF-TEM image shows the grain of fusiform (NbTi)C particles. (d) The region of the selected area electron diffraction pattern was collected from the region marked with a circle in (c).

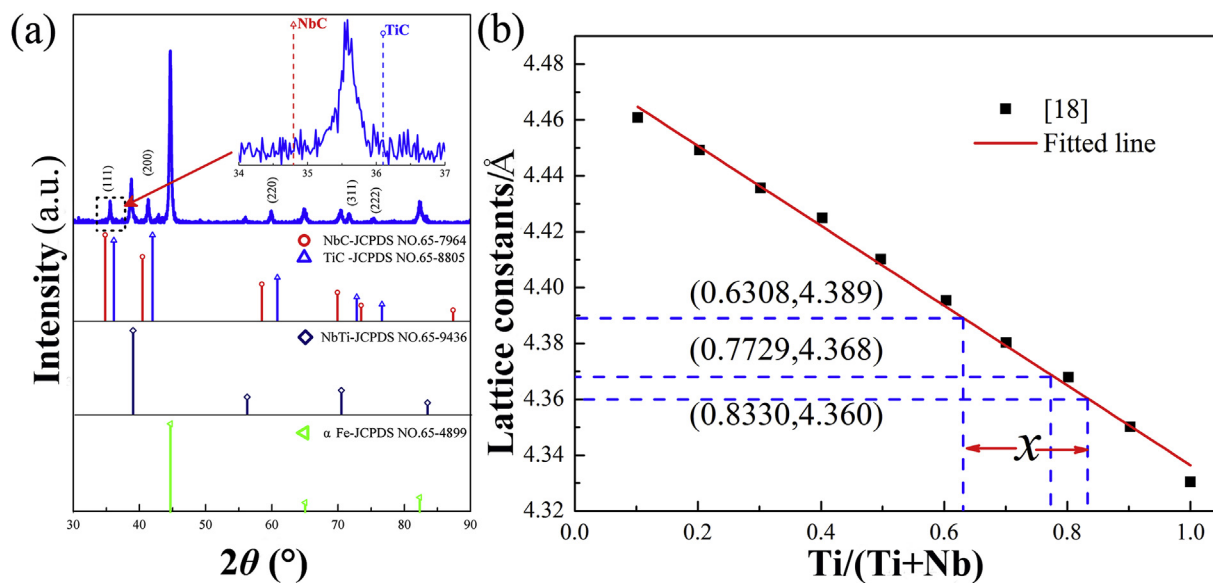
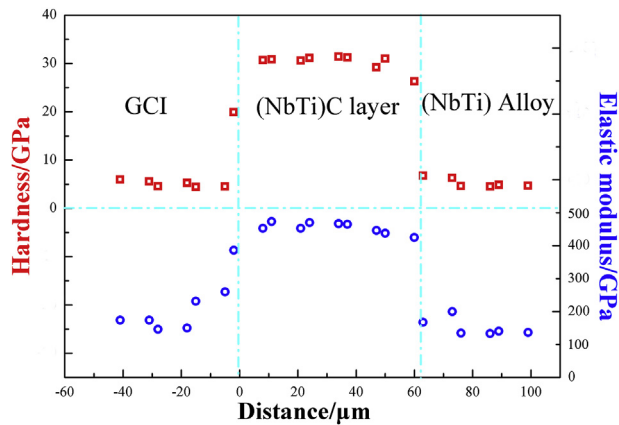


Fig. 5. (a) The XRD pattern of the NbTi-(NbTi)C-Fe composite and standard diffraction data. (b) the relationship between Ti/(Ti + Nb) ratio and lattice constant.

Table 2The 2θ values of different peaks of (NbTi)C and corresponding lattice constant.

Phase	2θ	Lattice constants(Å)	
NbC	34.796	4.462	JCPDS NO. 65-7964
(NbTi)C	35.39	4.389	Calculated with Eq. (1) and Eq. 2
	35.53	4.373	
	35.57	4.368	
	35.64	4.360	
	41.31	4.367	
	59.91	4.363	
TiC	36.099	4.306	JCPDS NO. 65-8805

**Fig. 6.** The variation of hardness near the cermet layer over a distance of 15 μm .

gray region is Nb-rich phase and the dark-gray region is Ti-rich phase. The EDS line scan of a single dark-gray particle from Zone-I, and EDS analysis of the areas marked with C and D, rendered the same results, as shown in Fig. 2(e) and Table 1. However, in Zone-II, the intensity of Ti is higher than Nb. The EDS scans from the areas, marked as A and B, near the NbTi/(NbTi)C-cermet interface exhibit that Ti and Nb atoms demonstrate long-range diffusion and obvious solute redistribution in Zone-II (Fig. 2(d) and Table 1). Hence, Zone-II consists of Ti-rich particles; the atomic fraction of Nb in NbTi region, which locate in the vicinity of NbTi/(NbTi)C interface, is higher than the raw material, as shown by the EDS analysis of region-A (Table 1).

The long-range diffusion of Nb and Ti atoms is derived by the difference in bonding force of Ti-C and Nb-C bonds. When C atoms diffuse into β -NbTi solid-solution, first, carbon atoms react with Ti due to the lower ΔG_{TiC} than ΔG_{NbC} [19]. Therefore, a part of the remaining Nb atoms is squeezed out towards the next reaction interface, which results in higher Nb content near the reaction interface than the raw NbTi material. Fig. 2(b) shows that Ti-rich and Nb-rich particles co-exist in Zone-I because the initial interface is in contact with GCI and C atoms rapidly diffused into the NbTi. Meanwhile, the diffusion of Nb and Ti atoms is much slower than the C atoms [18]. Therefore, Nb and Ti

atoms exhibited short-range diffusion. Hence, Zone-I consists of a mixture of Ti-rich and Nb-rich particles, as shown by dark-gray and light-gray particles in Fig. 2(e).

The image Fig. 2(f) indicates that the similar reinforced layer can be obtained from the experiment of vacuum furnace and EDS result indicate that the elemental composition of region-L is C, Ti, Nb, and Fe, it is same with the sample produced in argon gas furnace. But there is a high content of oxygen in the region-M (interface of (NbTi)C cermet layer/GCI), and the interface of (NbTi)C cermet layer/GCI is not well bonding. While the EDS result of the sample produced by argon gas furnace did not detect the oxygen. This result is caused that there still is the higher oxygen content under the vacuum degree of 0.05 MPa. If the vacuum degree is further improved, the sample quality will be further improved. However, the requirements for equipment will be further increased, which will increase the difficulty and economic cost of production. However, the better sample can be getting through the argon gas furnace, the argon gas furnace is easy manufacture, and there is a lower economic cost, meantime, the argon gas will not pollute the environment. Therefore, the argon gas furnace was chosen to produce the sample, and the subsequent research and analysis are the results of samples prepared by argon gas furnace.

The radial compression experiment was carried out to break the (NbTi)C cermet layer and the morphology of particles from different regions has been observed. Fig. 3(a) shows that Zone-I consists of dark gray fusiform particles and light gray near-spherical particles. The EDS analysis revealed that the light-gray sub-micron-sized particles are Nb-rich, whereas the dark-gray micron-sized particles are Ti-rich (Fig. 2(e)). Moreover, Zone-II is mainly composed of sub-micron-sized cubic or near-spherical particles.

Furthermore, corrosion extraction was used to analyze the three-dimensional morphology of various types of particles. (NbTi)C particles can be divided into two types: micron-sized fusiform particles and sub-micron-sized cubic or near-spherical particles, as shown in Fig. 3 (c) and (d). The fusiform particles correspond to the dark-gray particles in Zone-I, whereas the EDS scan from region E is consistent with the elemental composition of region C. The cubic or near-spherical particles have been observed in Zone-II, where the EDS scan of region F (Fig. 3(d)) is consistent with the EDS results of region B (Fig. 2(d)).

The EDS analysis reveals that (NbTi)C particles in different zones exhibit different Ti/(Nb + Ti) ratios, which can be ascribed to the redistribution of Nb and Ti during *in-situ* diffusion reaction. Therefore, TEM and XRD were used to further analyze and calculate the lattice constants of different particles and the relationship between the change in lattice constants and Ti/(Nb + Ti) ratio. Fig. 4(a) presents the bright-field (BF)-TEM image of near-spherical (NbTi)C particles. It can be seen that the particle diameter is ~ 500 nm, whereas the interplanar spacing 0.2223 nm corresponds to (002) planes of (NbTi)C (Fig. 4(b)). Fig. 4(c) shows the local BF-TEM image of fusiform particles, corresponding to the particles shown in Fig. 3(c). Herein, the interplanar spacing of 0.1549 nm corresponds to (220) planes of (NbTi)C (Fig. 4(d)).

Moreover, the lattice constant for the cubic crystal system can be calculated by using Eq. (1). The lattice constant values for the particles

Table 3as-calculated hardness of TiC, NbC and $(\text{Nb}_{0.25}\text{Ti}_{0.75})\text{C}$ phases.

Phase	Lattice constants	Possion ratio	Bulk modulus	Shear modulus	K = G/B	Hardness values
	a(Å)	ν	B(GPa)	G(GPa)		(GPa)
TiC	4.306 ^a	0.19 [22]	237 [23]	177 [24]	0.7468	25.78 ^[calculated]
(Nb _{0.25} Ti _{0.75})C	4.38 [17]	0.195 [17]	258 [17]	197 [17]	0.7635	28.51 [17]
NbC	4.462 ^b	0.22 [25]	318 [26]	198 [25]	0.6226	22.69 ^[calculated]
	—	—	—	—	—	23.5 [13]

^a -JCPDS NO.65-8805.^b -JCPDS NO.65-7964.

in Fig. 4(a) and c are $a_1 = 4.446 \text{ \AA}$ and $a_2 = 4.382 \text{ \AA}$, whereas the values for TiC and NbC are 4.306 \AA and 4.462 \AA , respectively. Therefore, the lattice constant values indicate that both particles fall in between the values of TiC and NbC. It can be qualitatively determined that the lattice constant of the fusiform particle, with higher Ti content, is closer to TiC.

$$\frac{1}{d^2} = \frac{h^2 + k^2 + l^2}{a^2} \quad (1)$$

$$2d\sin\theta = n\lambda \quad (2)$$

Moreover, XRD analysis was carried out to identify the phase composition of as-prepared sample produced at 1150°C for 6 h, and the results are presented in Fig. 5(a). The XRD patterns reveal that the composite is mainly composed of α -Fe, (NbTi)C and NbTi phase. By combining XRD and EDS results, it can be confirmed that the cermet layer is mainly composed of (NbTi)C phase. The 2θ positions of major diffraction peaks of (NbTi)C are located at 35.5° , 41.3° and 59.9° , which are located at the positions between TiC and NbC. The partially-enlarged XRD patterns indicate that multiple peaks exist at $2\theta \sim 35.5^\circ$ (Table 2), which can be ascribed to different substitutions of Ti and Nb in (NbTi)C phase. Therefore, instead of a single-phase region, the cermet layer consists of a (NbTi)C phase with different Ti/(Ti + Nb) ratios, which is consistent with EDS analysis.

Based on multiple peaks of (NbTi)C phase, the lattice constants of (NbTi)C phase, with different Ti/(Ti + Nb) ratios, have been calculated by using Eq. (1) and Eq. (2), as summarized in Table 2. The 2θ values of (111) plane range from 35.39° to 35.64° , and the corresponding lattice constants range from 4.389 \AA to 4.360 \AA (Table 2). At the same time, the diffraction peaks at 35.57° , 41.31° and 59.91° correspond to the maximum intensity peaks. One should note that the highest intensity peak is directly related to the phase content. The calculated results indicate that the lattice constants, corresponding to maximum intensity peaks, are similar, which implies that these three peaks correspond to the same phase. Rudy et al. have demonstrated that the lattice constants are almost linearly related to the exchange of Ti and Nb atoms [20]. Fig. 5(b) shows that the lattice constants of 4.389 \AA , 4.368 \AA and 4.360 \AA correspond to Ti/(Ti + Nb) ratio of 0.6308 , 0.7729 and 0.8330 , respectively. Hence, Ti/(Ti + Nb) ratio in (NbTi)C cermet layer ranged from 0.6308 to 0.8330 , whereas the ratio of major phases is 0.7729 , as shown as Fig. 5(b). One should note that these results are consistent with the EDS results in Table 1.

Furthermore, the hardness and elastic modulus near (NbTi)C cermet layer were evaluated by using nano-indenter, as shown in Fig. 6. The maximum hardness and elastic modulus of (NbTi)C cermet layer is 31.43 GPa and 473.11 GPa , respectively. On the other hand, the hardness and elastic modulus of NbTi alloy are 4.88 GPa and 139.89 GPa , whereas the hardness and elastic modulus of GCI are 5.96 GPa and 173.97 GPa , respectively. It is worth mentioning that the proposed method rendered higher hardness than TiC cermet (27.7 GPa) [14] and NbC cermet (23.5 GPa) [13]. The increased hardness corresponds to the solid solution strengthening due to the exchange of Ti and Nb atoms. Hence, the hardness of (NbTi)C cermet is mainly determined by the exchange of Ti and Nb atoms. Therefore, Tian et al.'s model (Eq. (3)) [21] is adopted to investigate the relationship between hardness and Ti/(Ti + Nb) ratio.

$$HV = 0.92K^{1.137}G^{0.708} \quad (3)$$

$$K = G/B \quad (4)$$

Where G refers to the shear modulus and B corresponds to the bulk modulus.

Table 3 shows that the theoretical hardness of TiC and NbC is 25.78 GPa and 22.69 GPa , respectively, and with the exchange of Ti and Nb atoms, the hardness of (TiNb)C will enhance obviously. The

(Nb_{0.25}Ti_{0.75})C exhibit a maximum hardness of 28.51 GPa [17]. Therefore, when the Ti/(Ti + Nb) ratio of (Nb_xTi_{1-x})C is about 0.75 , the (NbTi)C will possess the highest hardness.

According to the experimental results, (NbTi)C in the cermet layer possesses different ratios of Ti/(Ti + Nb). Based on XRD, EDS results and Rudy's research results, the Ti/(Ti + Nb) ratio of major phase of (NbTi)C is about 0.7729 , which is close to 0.75 . Combined with the calculated results, the formed (TiNb)C cermet layer will possess higher hardness. The hardness of the (TiNb)C cermet layer is 31.43 GPa , which is obviously higher than the TiC (27.7 GPa) and NbC (23.5 GPa).

Overall, (NbTi)C cermet layer exhibit the higher hardness than TiC and NbC cermets. Moreover, the remnant NbTi and ferrite zone, formed by decarbonizing, provides high plasticity, which can buffer and absorb high stress during the deformation process. Hence, the optimal combination of high hardness and excellent plasticity can effectively improve the overall performance of which composites.

4. Conclusions

In summary, *in-situ* solid-phase diffusion reaction has been successfully applied to fabricate NbTi-(NbTi)C Fe-based composites with a core-annular shell structure. The major phases of the as-prepared composites are α -Fe, NbTi and (NbTi)C. The reinforced cermet layer is composed of (NbTi)C, which exhibit different Ti/(Ti + Nb) ratios and vary with the carbon diffusion distance. Hence, the (NbTi)C cermet layer can be divided into two different zones; Zone-I exists in the vicinity of GCI and is composed of dark-gray fusiform micron-sized particles (Ti-rich) and light-gray cubic or near-spherical sub-micron-sized particles (Nb-rich). On the other hand, Zone-II exists near the NbTi layer and is composed of sub-micron-sized cubic or near-spherical particles. Moreover, Ti/(Ti + Nb) ratio in (NbTi)C cermet layer range from 0.6308 to 0.8330 , whereas the Ti/(Ti + Nb) ratio in major phase is 0.7729 . The maximum hardness of (NbTi)C cermet layer is 31.4 GPa , whereas the hardness of TiC and NbC is 27.7 GPa and 23.5 GPa , respectively. In the NbTi-(NbTi)C Fe-based composite, (NbTi)C cermet layer provides high hardness, whereas the remnant NbTi and ferrite zones formed by decarbonizing of GCI, which provide high plasticity and buffer the high plastic stress during deformation.

Acknowledgement

This work was supported by the Key-point Research and Invention Program of Shaanxi Province [Grant No. 2017ZDXM-GY-043] and the funding of the International Research Center for Composite and Intelligent Manufacturing Technology [Grant No. 2018GHJD-17] and Innovation Capability Support Program of Shaanxi Province (grant no. 2019-TD019).

References

- [1] B. Vishwanadh, A. Arya, R. Tewari, G.K. Dey, Formation mechanism of stable NbC carbide phase in Nb-1Zr-0.1C (wt.%) alloy, *Acta Mater.* 144 (2017) 470–483.
- [2] X.H. Wang, Z.D. Zou, S.Y. Qu, S.L. Song, Microstructure and wear properties of Fe-based hardfacing coating reinforced by TiC particles, *J. Mater. Process. Technol.* 168 (2005) 89–94.
- [3] J. Kim, M. Seo, S. Kang, Microstructure and mechanical properties of Ti-based solid-solution cermets, *Mater. Sci. Eng. A* 528 (2011) 2517–2521.
- [4] M.Y. Zhang, M. Li, J. Chi, S.F. Wang, L.S. Ren, M. Fang, C. Zhou, Microstructure evolution, recrystallization and tribological behavior of TiC/WC composite ceramics coating, *Vacuum* 166 (2019) 64–71.
- [5] W. Qiu, Y. Liu, J. Ye, H. Fan, Y. Qiu, Effects of (Ti,Ta,Nb,W)(C,N) on the microstructure, mechanical properties and corrosion behaviors of WC-Co cemented carbides, *Ceram. Int.* 43 (2017) 2918–2926.
- [6] H. Jiao, I.P. Jones, M. Aindow, Microstructures and mechanical properties of Nb-Ti-C alloys, *Mater. Sci. Eng. A* 485 (2008) 359–366.
- [7] Q. Li, Y. Lei, H. Fu, Laser cladding in-situ NbC particle reinforced Fe-based composite coatings with rare earth oxide addition, *Surf. Coat. Technol.* 239 (2014) 102–107.
- [8] Y.-b. Cao, H.-t. Ren, C.-s. Hu, Q.-x. Meng, Q. Liu, In-situ formation behavior of NbC-reinforced Fe-based laser cladding coatings, *Mater. Lett.* 147 (2015) 61–63.

- [9] H. Cao, X. Dong, S. Chen, M. Dutka, Y. Pei, Microstructure evolutions of graded high-vanadium tool steel composite coating in-situ fabricated via atmospheric plasma beam alloying, *J. Alloy. Comp.* 720 (2017) 169–181.
- [10] J. Jung, S. Kang, Sintered (Ti,W)C carbides, *Scr. Mater.* 56 (2007) 561–564.
- [11] J. Wang, Y. Wang, In-situ production of Fe–TiC composite, *Mater. Lett.* 61 (2007) 4393–4395.
- [12] X. Cai, Y. Xu, M. Liu, L. Zhong, F. Bai, Preparation of a gradient nanostructured surface TaC layer-reinforced Fe substrate by in situ reaction, *J. Alloy. Comp.* 712 (2017) 204–212.
- [13] N. Zhao, Y. Xu, W. Zhang, Z. Zhao, L. Zhong, Y. Fu, Gradually varying mechanical properties of in situ synthesized NbC–Fe-graded composite coating, *Mater. Sci. Technol.* 33 (2016) 220–226.
- [14] J. Zhu, L. Zhong, Y. Xu, X. Cai, F. Bai, Y. Ding, Z. Lu, H. Wu, Characterization and formation mechanisms of the TiC-Fe cermet layer in Ti–TiC–Fe composites, *Vacuum* 155 (2018) 631–636.
- [15] Z. Zhao, P. Hui, T. Wang, X. Wang, Y. Xu, L. Zhong, M. Zhao, New strategy to grow TiC coatings on titanium alloy: contact solid carburization by cast iron, *J. Alloy. Comp.* 745 (2018) 637–643.
- [16] M.Y. Zhang, M. Li, J. Chi, S.F. Wang, L.S. Ren, M. Fang, Microstructure and tribology properties of in-situ MC(M:Ti,Nb) coatings prepared via PTA technology, *Vacuum* 160 (2019) 264–271.
- [17] C. Zhao, Y. Zhou, X. Xing, L. Sha, X. Ren, Q. Yang, Precipitation stability and micro-property of (Nb, Ti)C carbides in MMC coating, *J. Alloy. Comp.* 763 (2018) 670–678.
- [18] Q. Li, Y. Lei, H. Fu, Growth mechanism, distribution characteristics and reinforcing behavior of (Ti, Nb)C particle in laser clad Fe-based composite coating, *Appl. Surf. Sci.* 316 (2014) 610–616.
- [19] A. Miriyev, M. Sinder, N. Frage, Thermal stability and growth kinetics of the interfacial TiC layer in the Ti alloy/carbon steel system, *Acta Mater.* 75 (2014) 348–355.
- [20] E. Rudy, Phase Equilibria Investigation of Binary, Ternary, and Higher Order Systems. Part VIII. The Structure of a Ternary Phase T3C2 in the V-TA-C System, (1970).
- [21] Y. Tian, B. Xu, Z. Zhao, Microscopic theory of hardness and design of novel superhard crystals, *Int. J. Refract. Metals Hard Mater.* 33 (2012) 93–106.
- [22] Y. Yang, H. Lu, C. Yu, J.M. Chen, First-principles calculations of mechanical properties of TiC and TiN, *J. Alloy. Comp.* 485 (2009) 542–547.
- [23] X. Fan, B. Chen, M. Zhang, D. Li, Z. Liu, C. Xiao, First-principles calculations on bonding characteristic and electronic property of TiC (111)/TiN (111) interface, *Mater. Des.* 112 (2016) 282–289.
- [24] K. Chen, L. Zhao, Elastic properties, thermal expansion coefficients and electronic structures of Ti_{0.75}X_{0.25}C carbides, *J. Phys. Chem. Solids* 68 (2007) 1805–1811.
- [25] L. Wu, Y. Wang, Z. Yan, J. Zhang, F. Xiao, B. Liao, The phase stability and mechanical properties of Nb–C system: using first-principles calculations and nano-indentation, *J. Alloy. Comp.* 561 (2013) 220–227.
- [26] J.H. Jang, C.-H. Lee, Y.-U. Heo, D.-W. Suh, Stability of (Ti,M)C (M=Nb, V, Mo and W) carbide in steels using first-principles calculations, *Acta Mater.* 60 (2012) 208–217.